TUDelft

Delft University of Technology

Integration of mass cytometry and mass spectrometry imaging for spatially resolved single-cell metabolic profiling

Nunes, Joana B.; Ijsselsteijn, Marieke E.; Abdelaal, Tamim; Ursem, Rick; van der Ploeg, Manon; Giera, Martin; Everts, Bart; Mahfouz, Ahmed; Heijs, Bram; de Miranda, Noel F.C.C.

Important note
To cite this publication, please use the final published version (if applicable).
Please check the document version above.

Integration of mass cytometry and mass spectrometry imaging for spatially resolved single-cell metabolic profiling

Check for updates

Joana B. Nunes [1,9], Marieke E. Ijsselsteijn [1,9], Tamim Abdelaal[2,3,4], Rick Ursem [1,5], Manon van der Ploeg[1], Martin Giera [5,6], Bart Everts [7], Ahmed Mahfouz [4,8], Bram Heijs[5,6,9] & Noel F. C. C. de Miranda [1,9] ✉

The integration of spatial omics technologies can provide important insights into the biology of tissues. Here we combined mass spectrometry imaging-based metabolomics and imaging mass cytometry-based immunophenotyping on a single tissue section to reveal metabolic heterogeneity at single-cell resolution within tissues and its association with specific cell populations such as cancer cells or immune cells. This approach has the potential to greatly increase our understanding of tissue-level interplay between metabolic processes and their cellular components.

Metabolism is an essential aspect of biological systems that must be considered to comprehend tissue homeostasis and pathogenesis[1,2]. Single-cell proteomic and transcriptomic analyses have substantially advanced our understanding of metabolic variations across different cell populations, particularly immune cells, to uncover metabolic heterogeneity as well as explore links between cell phenotypes and metabolic profiles[3-5]. Most de facto single-cell analysis approaches extract cells from their natural context and, thus, lack spatially resolved information and disregard cellular interactions. Furthermore, the reliance on surrogate markers, such as enzymes or their transcripts may provide an inadequate representation of metabolic states. Imaging mass cytometry (IMC) and mass spectrometry imaging (MSI)-based spatial metabolomics are increasingly being utilized for the multiplexed detection of cellular markers and metabolites, respectively, while preserving the spatial context of tissues[6].

We developed a novel multimodal MSI approach for the integrated analysis of metabolites and immunophenotypes in human tissues. This was achieved by integrating the experimental workflows and the data generated from spatial metabolomics using matrix-assisted laser desorption/ionization MSI (MALDI-MSI) and multiparameter spatial

immunophenotyping by IMC. We developed and optimized a wet-lab protocol that allows the application of both technologies on the same tissue section. Additionally, we have implemented a data integration strategy that enables the relative quantification of metabolites (measured by MALDI-MSI) at the single-cell level (defined by IMC) (Fig. 1a).

Spatial immunophenotyping and per-cell metabolite analysis were accomplished by combining MALDI-MSI with IMC on the same tissue section. Details on the optimization of this methodology can be found in Supplementary Notes and Supplementary Figs. 1 and 2. Briefly, MALDI-MSI can be followed by IMC on 5 μm tissue sections, as opposed to the typical 10 μm sections used for MALDI-MSI. This is achieved by using an IMC antibody panel for formalin-fixed paraffin-embedded tissues (Supplementary Table 1 (ref. 7)) combined with a formalin fixation step after matrix removal.

We applied our optimized protocol on three tumor samples, including one mismatch repair-deficient colorectal cancer (CRC1). To merge the output data from MALDI-MSI and IMC, we performed image coregistration based on visual features that contained recognizable landmarks such as empty areas or epithelial structures (Extended Data Fig. 1a). However, owing to the pixel size differences between

[1]Department of Pathology, Leiden University Medical Center, Leiden, The Netherlands. [2]Department of Radiology, Leiden University Medical Center, Leiden, The Netherlands. [3]Systems and Biomedical Engineering Department, Faculty of Engineering Cairo University, Giza, Egypt. [4]Pattern Recognition and Bioinformatics, Delft University of Technology, Delft, The Netherlands. [5]Center for Proteomics and Metabolomics, Leiden University Medical Center, Leiden, The Netherlands. [6]The Novo Nordisk Foundation Center for Stem Cell Medicine (reNEW), Leiden University Medical Center, Leiden, The Netherlands. [7]Center of Infectious Diseases, Leiden University Medical Center, Leiden, The Netherlands. [8]Department of Human Genetics, Leiden University Medical Center, Leiden, The Netherlands. [9]These authors contributed equally: Joana B. Nunes, Marieke E. Ijsselsteijn, Bram Heijs, Noel F. C. C. de Miranda. ✉e-mail: N.F.de_miranda@lumc.nl

MALDI-MSI and IMC, it was necessary to adjust for these variations to determine metabolite abundance at the single-cell level. To accomplish this, we assigned the metabolite abundance of each MALDI-MSI pixel to the corresponding overlapping 25 IMC pixels (Methods and Extended Data Fig. 1b). Cells were identified through cell segmentation by using the DNA, keratin (epithelial cells) and vimentin (stromal cells) images derived from the IMC data[8]. Subsequently, using the previously assigned pixel metabolite abundance, we calculated the relative metabolite abundance per cell. Additionally, by leveraging the cell marker expression from the IMC data, we identified a total of 22 cellular phenotypes, including cancer cells, macrophages and T cells (Extended Data Fig. 1c). Given that MALDI-MSI pixels measure 5×5 μm, a single MSI pixel may encompass multiple cells, potentially leading to mixed metabolite profiles being assigned to different cells. However, our observations revealed that ~30% of MSI pixels in regions with tissue typically contained only one cell (Extended Data Fig. 1d).

Using trapped ion mobility separation (TIMS), we identified and named 112 metabolites, mainly glycerophospholipids, from the MALDI-MSI data (Supplementary Table 3). Employing these glycerophospholipids as features, we conducted a hierarchical clustering analysis across the 22 identified cell populations. This analysis revealed that distinct cell types, such as cancer cells, plasma B cells and CD204+ macrophages, showed varying abundances of glycerophospholipid features (Fig. 1b and Extended Data Fig. 1e). To delve deeper, we focused on the CRC1 sample, notable for its high immune infiltration, in line with its mismatch repair-deficient status. We performed Uniform Manifold Approximation and Projection (UMAP) dimensionality reduction on all cells, and specifically on immune cells, using metabolite abundances as features (Fig. 1c,d). Consistent with the distinct metabolite profiles observed in Fig. 1b, cancer cells were separated from stromal–immune cells in the UMAP embedding (Fig. 1c and Extended Data Fig. 2a,b). This separation was supported by a greater pairwise distance between the metabolite abundance profiles of cancer cells versus stromal and immune cells as compared with within these compartments (Extended Data Fig. 2b). To discern glycerophospholipids with differential abundances between cancer cells and stromal–immune cells, we calculated fold changes between these subsets (Fig. 1e). Notably, phosphatidylcholine PC(37:5) was found to be most differentially abundant in the stromal–immune compartment, while phosphatidylinositol PI(34:1) was predominantly present in cancer cells. This was corroborated by the fact that the spatial localization of these lipid molecules was found to be highly overlapping with the one of keratin (for cancer cells) or vimentin (for the stromal–immune cell compartment) (Fig. 1f). Both PI(34:1) and PC(37:5) have been described to be upregulated in cancer[9,10]. Interestingly, while PI(34:1) is known to be abundant in CRC cell lines[11], comprehensive data on lipid profiles in the context of the tumor microenvironment remains limited.

In the immune cell compartment, only a few immune cell subsets, notably plasma B cells, were grouped by cell type on the basis of their metabolic features (Fig. 1d). This observation suggests variability in metabolic processes across most immune cell populations. By using a confusion matrix, we investigated whether k-means clustering of immune cells, using glycerophospholipid features, resulted in clusters driven by the distinct immune cell types. Except for plasma B cells, no association was found (Extended Data Fig. 2c,d). Interestingly, even though CD204+ macrophages did not form a distinct cluster in the UMAP embedding (Fig. 1d), they displayed a distinctive glycerophospholipid profile in the hierarchical clustering heatmap (Fig. 1b). Therefore, we delved into the unique glycerophospholipid profiles of CD204+ macrophages by comparing those with the ones from the remaining immune and stromal cells. This analysis revealed several glycerophospholipids, notably phosphatidylglycerole PG(40:7) and lysophosphatidylinositol LPI(18:1), that were more abundant in CD204+ macrophages (Fig. 2a,b). Interestingly, LPI(18:1) has been suggested to play a role in cancer as lysophosphatidylinosytols induce ERK1/2 phosphorylation via the GPR55 receptor[12,13].
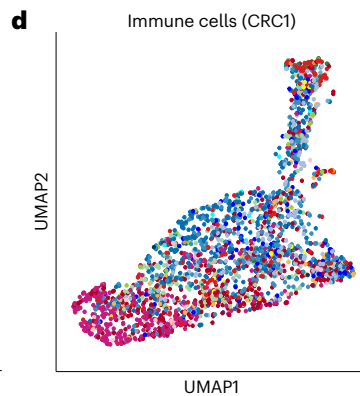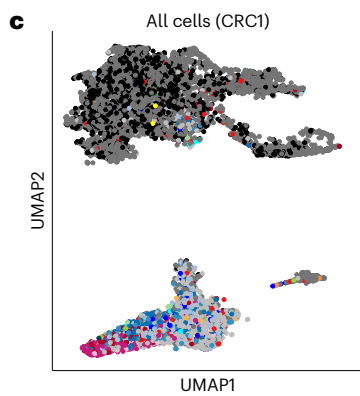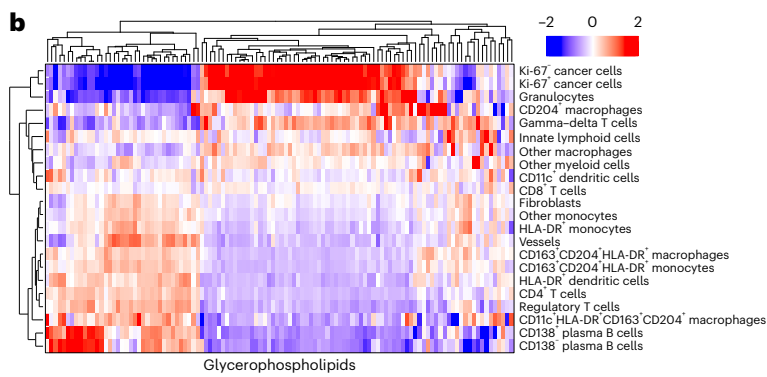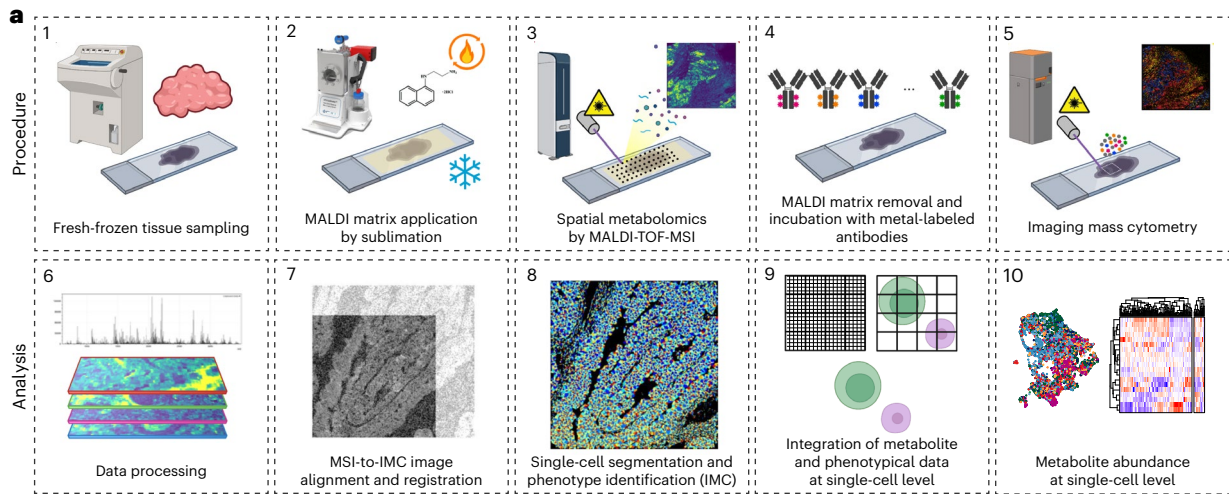
We further explored if distinct glycerophospholipid profiles could be identified in the macrophage compartment that are independent of the assigned phenotypes. By applying k-means clustering to macrophages and monocyte populations based on glycerophospholipid features, we were able to distinguish various clusters within this compartment (Fig. 2c–e). For instance, cluster 8 was marked by high abundance of phosphatidylethanolamine PE(O-36:5), PE(O-38:5) and phosphatidic acid PA(36:1), which were scarcely present in other clusters (Fig. 2e and Extended Data Fig. 3). Overall, the multimodal imaging and analysis approach used in this study not only facilitates the evaluation of metabolites at the single-cell resolution but also underscores the existence of glycerophospholipid abundance differences both between and within cellular phenotypes. Furthermore, our observation of cell-specific lipid signatures resonates with the recently proposed 'lipotype hypothesis', which suggests a bidirectional connection between transcriptional states and lipid signatures. This finding highlights the importance of multimodal, spatially resolved single-cell analyses[14].
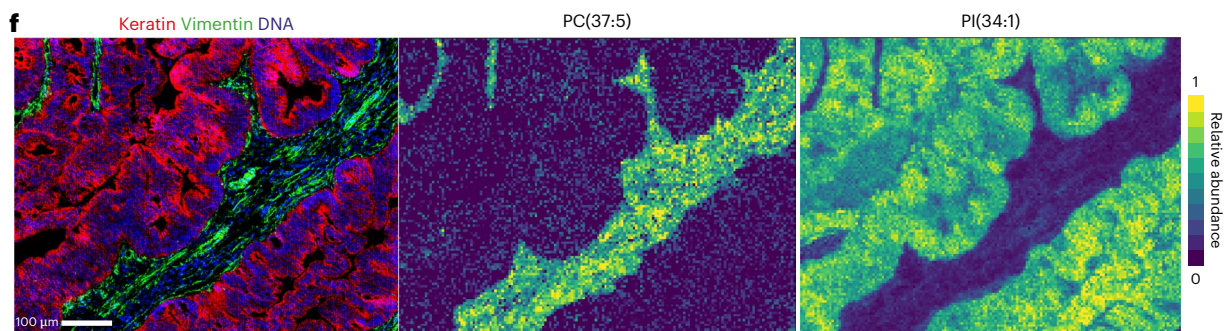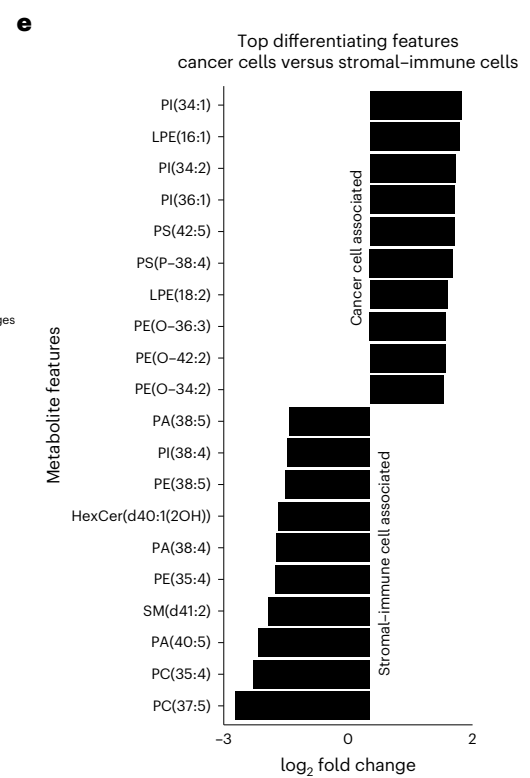
Discussion

Substantial advancements have been made in using MSI for single-cell metabolic characterization in cancer research[15]. However, a major challenge remains in profiling the metabolism of immune cells within the complex tumor microenvironment. Past efforts have combined MALDI-MSI with immunofluorescence (IF) or IMC on consecutive tissue sections, but data integration can be challenging[16,17]. Alternatives, such as performing immunohistochemistry (IHC) or IF after MALDI-MSI on the same section, are limited by the number of targets they can assess[18–20]. Although desorption electrospray ionization MSI as well as time-of-flight (TOF) secondary ion mass spectrometry have been combined with IMC on the same tissue section, they are hindered by limited spatial resolution or sensitivity respectively[21,22]. The MALDI-IHC technique, while similar, also faces issues with spatial resolution for immunophenotyping compared with IMC[23,24]. Recent studies have used formalin-fixed paraffin-embedded tissue for combining IMC and MSI owing to better preservation of tissue architecture and antibody performance, but the use of fixated tissue complicates the detection of several metabolites[22,25]. In our study, we introduce an optimized workflow that utilizes fresh frozen tissue, combining MALDI-MSI for metabolite detection with IMC for cellular phenotype identification

Fig. 1 | Identification of single-cell metabolic profiles in CRC. a, Integrated workflow of consecutive MALDI-MSI and IMC analyses. Fresh-frozen tissue sections were cut (1) and treated with MALDI matrix (2). MALDI-TOF-MSI was performed to obtain spatial metabolomics data (3), followed by matrix removal (4). Sections were then labeled with metal-conjugated antibodies, and IMC was used to analyze the areas previously imaged by MALDI-TOF-MSI (5). Both datasets were preprocessed (6) and coregistered using visual landmarks (7). Cell segmentation and phenotype identification were performed (8), and MALDI-MSI-derived metabolic abundances were assigned to each cell (9), enabling downstream analysis (10). Created with BioRender.com. **b**, Scaled metabolite abundance profiles ac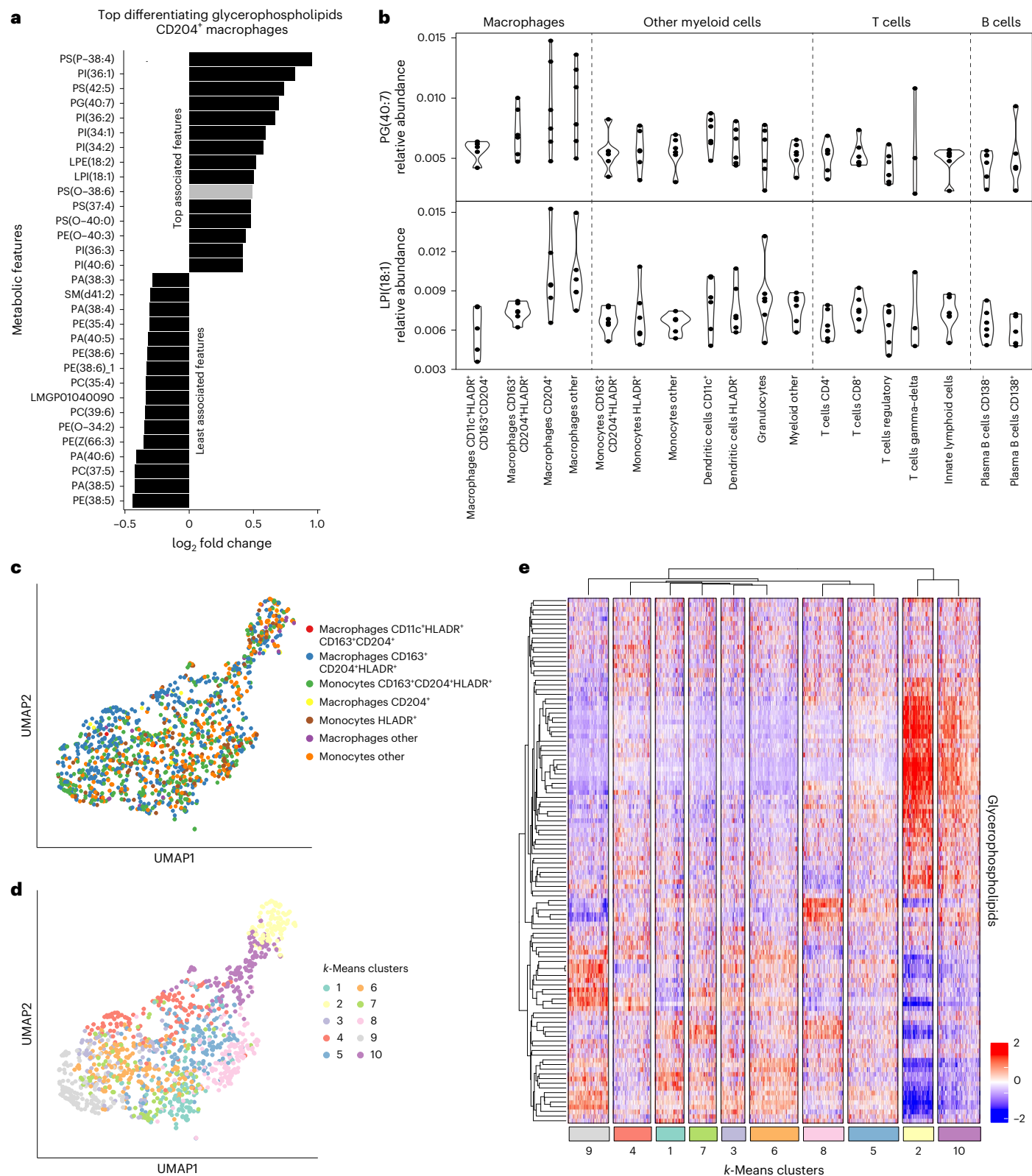ross cell populations identified in CRC1. Hierarchical clustering was guided by glycerophospholipid abundances (heatmaps of CRC2 and CRC3 are shown in Extended Data Fig. 1e). **c,d**, UMAP embedding of all cells (**c**) or immune cells (**d**) of CRC1, clustered by glycerophospholipids. Phenotypes of labeled cells are visualized on the UMAP embedding. **e**, Top differentiating glycerophospholipid features between cancer cells and the stromal–immune cell compartment, calculated for all images in the dataset. **f**, Left: representative IMC image of CRC1 highlighting cancer cells and stromal cells (keratin in red, vimentin in green and DNA in blue). Middle and right: MALDI-MSI image of the same region of interest showing differentially abundant metabolites in the stromal–immune cell compartment (PC(37:5)) and in cancer cells (PI(34:1)) displayed using viridis colors with saturated pixels above the 99th percentile ($n = 2$).

a Procedure

1. Fresh-frozen tissue sampling
2. MALDI matrix application by sublimation
3. Spatial metabolomics by MALDI-TOF-MSI
4. MALDI matrix removal and incubation with metal-labeled antibodies
5. Imaging mass cytometry

Analysis

6. Data processing
7. MSI-to-IMC image alignment and registration
8. Single-cell segmentation and phenotype identification (IMC)
9. Integration of metabolite and phenotypical data at single-cell level
10. Metabolite abundance at single-cell level

b

Glycerophospholipids

Ki-67⁻ cancer cells
Ki-67⁺ cancer cells
Granulocytes
CD204⁺ macrophages
Gamma–delta T cells
Innate lymphoid cells
Other macrophages
Other myeloid cells
CD11c⁺ dendritic cells
CD8⁺ T cells
Fibroblasts
Other monocytes
HLA-DR⁺ monocytes
Vessels
CD163⁺CD204⁺HLA-DR⁺ macrophages
CD163⁺CD204⁺HLA-DR⁺ monocytes
HLA-DR⁺ dendritic cells
CD4⁺ T cells
Regulatory T cells
CD11c⁺HLA-DR⁺CD163⁺CD204⁺ macrophages
CD138⁺ plasma B cells
CD138⁻ plasma B cells

c All cells (CRC1)

UMAP2 / UMAP1

d Immune cells (CRC1)

UMAP2 / UMAP1

e Top differentiating features cancer cells versus stromal–immune cells

Cancer cell associated:
PI(34:1)
LPE(16:1)
PI(34:2)
PI(36:1)
PS(42:5)
PS(P–38:4)
LPE(18:2)
PE(O–36:3)
PE(O–42:2)
PE(O–34:2)

Stromal–immune cell associated:
PA(38:5)
PI(38:4)
PE(38:5)
HexCer(d40:1(2OH))
PA(38:4)
PE(35:4)
SM(d41:2)
PA(40:5)
PC(35:4)
PC(37:5)

Metabolite features / log₂ fold change

Legend:
- Ki-67⁻ cancer cells
- Ki-67⁺ cancer cells
- Fibroblasts
- Vessels
- CD4⁺ T cells
- CD8⁺ T cells
- FOXP3⁺ T cells
- Gamma–delta T cells
- Innate lymphoid cells
- CD138⁺ plasma B cells
- CD138⁻ plasma B cells
- CD11c⁺ dendritic cells
- HLA-DR⁺ dendritic cells
- Granulocytes
- Other macrophages
- Other monocytes
- HLA-DR⁺ monocytes
- CD11c⁺HLA-DR⁺CD163⁺CD204⁺ macrophages
- CD163⁺CD204⁺HLA-DR⁺ macrophages
- CD163⁺CD204⁺HLA-DR⁺ monocytes
- CD204⁺ macrophages

f Keratin Vimentin DNA | PC(37:5) | PI(34:1)

100 μm

Relative abundance 0–1

Fig. 2 | Glycerophospholipid landscape of myeloid cells. a, Differential glycerophospholipid features distinguishing CD204⁺ macrophages from other cells in the stroma, calculated for all images in the dataset. Differentially abundant metabolites were identified by Wilcoxon test, and features with a FDR-adjusted P value below 0.05 are shown in black. **b**, Violin plots showing the relative abundance per cell of the two most differentially abundant metabolites in CD204⁺ macrophages. Each dot represents an image. **c**, UMAP embedding of macrophages/monocytes in CRC1, utilizing glycerophospholipids as features. Cells are labeled by IMC phenotypes. **d**, k-Means clusters of macrophages/monocytes based on glycerophospholipids, visualized on the UMAP embedding of **c**. **e**, The relative abundance of glycerophospholipids in the k-means clusters, visualized in **d** (enlarged heatmap with metabolite annotation is available in Extended Data Fig. 3).

on a single tissue section. This method overcomes previous challenges with image alignment and can be directly applied to various tissue types to characterize the metabolite composition of single cells in situ. Limitations of the work described here include the small sample size, which limits the interpretability of the findings, and the specific focus on glycerophospholipids. However, by adjusting the range of the mass spectrometer, this approach can analyze the entire metabolic spectrum. Additionally, to fully explore metabolic heterogeneity in specific immune cells, the current 26-target IMC panel can be expanded to include more than 40 cellular targets, allowing for the identification of more immune subsets and states. In summary, our method provides a powerful tool for tissue characterization, simultaneously revealing cellular composition and directly linking it to metabolic phenotypes. This is particularly valuable to be applied in complex systems like the tumor microenvironment, where cellular composition and metabolism have a high degree of heterogeneity.

Online content

Any methods, additional references, Nature Portfolio reporting summaries, source data, extended data, supplementary information, acknowledgements, peer review information; details of author contributions and competing interests; and statements of data and code availability are available at https://doi.org/10.1038/s41592-024-02392-6.

References

1. Wang, G. et al. Spatial dynamic metabolomics identifies metabolic cell fate trajectories in human kidney differentiation. *Cell Stem Cell* **29**, 1580–93 e7 (2022).
2. Pavlova, N. N., Zhu, J. & Thompson, C. B. The hallmarks of cancer metabolism: still emerging. *Cell Metab.* **34**, 355–377 (2022).
3. Hrovatin, K., Fischer, D. S. & Theis, F. J. Toward modeling metabolic state from single-cell transcriptomics. *Mol. Metab.* **57**, 101396 (2022).
4. Artyomov, M. N. & Van den Bossche, J. Immunometabolism in the single-cell era. *Cell Metab.* **32**, 710–725 (2020).
5. Purohit, V., Wagner, A., Yosef, N. & Kuchroo, V. K. Systems-based approaches to study immunometabolism. *Cell Mol. Immunol.* **19**, 409–420 (2022).
6. Lewis, S. M. et al. Spatial omics and multiplexed imaging to explore cancer biology. *Nat. Methods* **18**, 997–1012 (2021).
7. Ijsselsteijn, M. E., van der Breggen, R., Farina Sarasqueta, A., Koning, F. & de Miranda, N. A 40-marker panel for high dimensional characterization of cancer immune microenvironments by imaging mass cytometry. *Front. Immunol.* **10**, 2534 (2019).
8. Ijsselsteijn, M. E., Somarakis, A., Lelieveldt, B. P. F., Hollt, T. & de Miranda, N. Semi-automated background removal limits data loss and normalizes imaging mass cytometry data. *Cytometry A* **99**, 1187–1197 (2021).
9. Owusu Obeng, E. et al. Phosphoinositide-dependent signaling in cancer: a focus on phospholipase C isozymes. *Int. J. Mol. Sci.* **21**, 2581 (2020).
10. Chen, Y. et al. Simultaneous quantification of serum monounsaturated and polyunsaturated phosphatidylcholines as potential biomarkers for diagnosing non-small cell lung cancer. *Sci. Rep.* **8**, 7137 (2018).
11. Elmallah, M. I. Y. et al. Lipidomic profiling of exosomes from colorectal cancer cells and patients reveals potential biomarkers. *Mol. Oncol.* **16**, 2710–2718 (2022).
12. Calvillo-Robledo, A., Cervantes-Villagrana, R. D., Morales, P. & Marichal-Cancino, B. A. The oncogenic lysophosphatidylinositol (LPI)/GPR55 signaling. *Life Sci.* **301**, 120596 (2022).
13. Masquelier, J. et al. Lysophosphatidylinositols in inflammation and macrophage activation: altered levels and anti-inflammatory effects. *Biochim. Biophys. Acta Mol. Cell. Biol. Lipids* **1863**, 1458–1468 (2018).
14. D'Angelo, G. & La Manno, G. The lipotype hypothesis. *Nat. Rev. Mol. Cell Biol.* **24**, 1–2 (2023).
15. Liu, J., Hu, W., Han, Y. & Nie, H. Recent advances in mass spectrometry imaging of single cells. *Anal. Bioanal. Chem.* **415**, 4093–4110 (2023).
16. Tuck, M., Grelard, F., Blanc, L. & Desbenoit, N. MALDI-MSI towards multimodal imaging: challenges and perspectives. *Front. Chem.* **10**, 904688 (2022).
17. Goossens, P. et al. Integrating multiplex immunofluorescent and mass spectrometry imaging to map myeloid heterogeneity in its metabolic and cellular context. *Cell Metab.* **34**, 1214–25 e6 (2022).
18. Kaya, I. et al. Histology-compatible MALDI mass spectrometry based imaging of neuronal lipids for subsequent immunofluorescent staining. *Anal. Chem.* **89**, 4685–4694 (2017).
19. Dufresne, M. et al. Multimodal detection of GM2 and GM3 lipid species in the brain of mucopolysaccharidosis type II mouse by serial imaging mass spectrometry and immunohistochemistry. *Anal. Bioanal. Chem.* **409**, 1425–1433 (2017).
20. Rappez, L. et al. SpaceM reveals metabolic states of single cells. *Nat. Methods* **18**, 799–805 (2021).
21. Strittmatter, N. et al. Method to visualize the intratumor distribution and impact of gemcitabine in pancreatic ductal adenocarcinoma by multimodal imaging. *Anal. Chem.* **94**, 1795–1803 (2022).
22. Hu, T. et al. Single-cell spatial metabolomics with cell-type specific protein profiling for tissue systems biology. *Nat. Commun.* **14**, 8260 (2023).
23. Yagnik, G., Liu, Z., Rothschild, K. J. & Lim, M. J. Highly multiplexed immunohistochemical MALDI-MS imaging of biomarkers in tissues. *J. Am. Soc. Mass. Spectrom.* **32**, 977–988 (2021).
24. Lim, M. J. et al. MALDI HiPLEX-IHC: multiomic and multimodal imaging of targeted intact proteins in tissues. *Front. Chem.* **11**, 1182404 (2023).
25. Dunne, J. et al. Evaluation of antibody-based single cell type imaging techniques coupled to multiplexed imaging of N-glycans and collagen peptides by matrix-assisted laser desorption/ionization mass spectrometry imaging. *Anal. Bioanal. Chem.* **415**, 7011–7024 (2023).

Methods

Sample collection and sampling

Material was used of three CRCs from patients that have given informed consent under the study protocol P15.282, approved by the Medical Ethical Committee of the Leiden University Medical Centre. Patient samples were anonymized and handled according to the medical ethical guidelines described in the Code of Conduct for Proper Secondary Use of Human Tissue of the Dutch Federation of Biomedical Scientific Societies. After surgery, cancer tissue was snap-frozen and stored at −80 °C.

Using a micro cryostat (CM3050 S, Leica), 5-µm-thick tissue sections were thaw-mounted on indium-tin-oxide (ITO)-coated microscope slides (Bruker Daltonics GmbH) and immediately processed for MALDI-MSI analysis.

MALDI-MSI

Samples from the cryomicrotome were transferred on dry ice and equilibrated to room temperature using a vacuum freeze drier (Alpha 2-4 LSCbasic, Christ) for 20 min. Following, the MALDI matrix, 1-napthyll ethylenediamine dihydrochloride was sublimated onto the slide using a Sublimator T1 (HTX Imaging). Sublimation was performed at 180 °C for 6 min, which resulted in a matrix coverage of 31.73 pmol mm^{-2}. MSI analyses was performed on a timsTOF fleX MALDI-2 platform with microGRID (Bruker Daltonics GmbH) in both oTOF and timsON modes. To achieve single-cell resolution, single-pixel mass spectra were recorded in oTOF mode at a 5×5 µm^2 spatial resolution covering a m/z range between 300 and 1,100, and summing 25 laser shots. For collisional cross-section (CCS)-enhanced identification of m/z features, single-pixel mass spectra were recorded in timsON mode at a 10×10 µm^2 spatial resolution covering a m/z range between 300 and 1,100 and summing 74 laser shots. Ion mobility separation was achieved over a 300 ms ramp over a $1/K_0$ interval ranging from 0.6 to 1.6 V s^{-1} cm^{-2}. The flexImaging software (v7.2, Bruker Daltonics) was used to define measurement regions of approximately 1×1 mm^2 for oTOF mode measurements, and regions of approximately 0.5×1 mm^2 for consecutive timsON and oTOF mode measurements. Post measurement, samples were immediate processed for the IMC analysis. Raw data files were loaded into SCiLS Lab PRO software (v2024a, Bruker Daltonics). Two separate files were created, one with timsON data for molecular annotations, and one with oTOF data for visualization at the single-cell level. Feature selection was performed in the timsON dataset by using the T-ReX[3] feature finding algorithm in SCiLS Lab (parameters: neighborhood size 4×4, coverage 100%, relative intensity threshold 0.3%). CCS-aware molecular annotation was performed against a subset of the Lipid Maps Structural Database (lipid classes: glycerophospholipids (GP) and glycosphingolipids (SP); https://HMDB.ca (ref. 26)) using the MetaboScape (v2023b, Bruker Daltonics) target list annotation tool, directly accessed by SCiLS Lab (parameters: Enabled CCS-Predict Pro, m/z narrow 5.0 ppm, m/z wide 15.0 ppm, mSigma_narrow 100, mSigma_wide 900, CCS_narrow 2.0%, CCS_wide 4.0%). Following molecular annotation, only deprotonated molecular ions ([M − H$^+$]$^-$) with a mass error tolerance below 10 ppm and a CCS error tolerance below 5% were selected and considered for further analysis. The m/z intervals ($m/z \pm 6.6$ ppm) of the selected features in the timsON dataset were transferred to the oTOF dataset, from which single-ion images at single-cell resolution were exported as OME-TIFF images for every individual measurement area.

IMC

After MALDI-MSI data acquisition, excess MALDI matrix was removed by washing the tissue slides with 100% ethanol, ice-cold acetone, 100% ethanol and 70% ethanol for 5 min each, followed by a 2-min wash with 50% ethanol and 3× 1-min washes with 1× phosphate-buffered saline. The tissues were then fixed with 10% formalin for 1 h at room temperature. Antigen retrieval, blocking and labeling with metal-conjugated antibodies (Supplementary Table 1) was performed as previously described by IJsselsteijn et al.[7]. The utilized panel has been applied to various studies and was validated after conjugation by IHC and through assessment of colocalization with expected other markers by IMC. To obtain the data in Supplementary Fig. 1b, tissue fixation was performed after excess MALDI matrix removal with 4% paraformaldehyde for 30 min at 4 °C and the IMC staining according to the protocol of Guo et al.[27]. Data from $1,100 \times 1,100$ µm^2 areas was acquired using a Hyperion Mass Cytometry System (Standard BioTools) and CyTOF software (7.0.5189, Standard Biotools), exported as .mcd files and visualized using MCD Viewer (1.0.5, Standard BioTools).

Phenotype identification and counting was done as described previously[8]. In short, .mcd files were converted to TIFF images and normalized by saturating pixels above the 99th percentile. Next, background removal was performed using the random forest classifier of Ilastik after which all remaining pixels were binarized to 1, with background set to 0. Cell segmentation masks were created using Ilastik and CellProfiler using the keratin, vimentin/CD45 and DNA images, and marker intensities per cell were extracted using ImaCytE. Cells were analyzed by t-distributed stochastic neighbor embedding in Cytosplore, and by mean-shift clustering, cells forming visual neighborhoods in the t-distributed stochastic neighbor embedding were grouped to define cellular phenotypes. Cell types were defined on the basis of current literature using the protein markers described in Supplementary Table 2. Furthermore, all identified phenotypes were visually confirmed on the raw images. RStudio (2022.07.1, R version 4.2.0) was used for the counting of phenotypes per sample and visual representation.

MSI and IMC data integration

For each tumor sample, MALD-MSI and IMC data were combined in Python (version 3.9), by coregistering the two image sets based on visual features in both datasets showing clear landmarks, such as empty areas or epithelial structures. Excess pixels, which can be found on the borders of the images belonging only to one dataset, were excluded, retaining only coregistered pixels. Since MALDI-MSI resolution is 5×5 µm^2 and IMC resolution is 1×1 µm^2, each MALDI-MSI pixel maps to 25 IMC pixels.

Cells often do not exactly overlap with one MALDI-MSI pixel and can cover only part or several MALDI-MSI pixels. To calculate metabolite abundance per cell, the peak intensity of the overlapping 5×5 µm MALDI-MSI pixel was assigned to each 1×1 µm IMC pixel. The IMC cell segmentation mask and the assigned peak intensities of each 1×1 µm were combined, and the relative metabolite abundance per cell was calculated using the mean of all pixels within a cell. For instance, if a cell consists of 10 IMC pixels, and 5 of those fall into a MALDI-MSI pixel with peak intensity 1, and 5 IMC pixels fall in a MALDI-MSI pixel with peak intensity 0, then the mean intensity of the cell is $(5 \times 1) + (5 \times 0)/10 = 0.5$ (exemplified in Extended Data Fig. 1b).

In mathematical terms: let $X_i = \{x_1, x_2, \ldots, x_N\}$ be the set of IMC pixels, where N is the total number of coregistered pixels, and $Y_j = \{y_1, y_2, \ldots, y_M\}$ be the set of MALDI-MSI pixels, where M is the total number of coregistered pixels, such that $M = N/25$. Each y_j maps to 25 x_is, while x_i maps to (is part of) a single y_j; therefore, $y_j = f(x_i)$, where $f()$ is a defined mapping function returning the corresponding y_j pixel for the input x_i pixel.

For both modalities, each pixel represents a one-dimensional vector containing the features measured by that modality. Cells were segmented using the high-resolution IMC dataset; let $C_k = \{c_1, c_2, \ldots, c_k\}$ be the set of segmented cells, and n is the total number of cells. Each cell c_k is a set of several IMC pixels x_is, while one IMC pixel x_i is part of only one cell. To obtain the cellular IMC expression data, we define

$$\bar{P}_{k,p} = \frac{1}{m_k} \sum_{i=1}^{m_k} P_{i,p},$$

where $\bar{P}_{k,p}$ is the cellular expression of IMC protein feature p in cell c_k, $P_{i,p}$ is the pixel expression of protein feature p in IMC pixel x_i, and m_k is the number of IMC pixels corresponding to cell c_k. In other words, the cellular expression of the IMC data is the average expression of the IMC pixels corresponding to each cell. Similarly, let $T_{j,t}$ be the pixel expression of metabolic feature t in pixel y_j; therefore,

$$\bar{T}_{k,t} = \frac{1}{m_k} \sum_{i=1}^{m_k} T_{f(i),t},$$

where $\bar{T}_{k,t}$ is the cellular expression of metabolic feature t in cell c_k, and $T_{f(i),t}$ the pixel expression of metabolic feature t in MALDI-MSI pixel mapping to IMC pixel x_i. In other words, the cellular expression of the MALDI-MSI data is the weighted-average expression of the MALDI-MSI pixels corresponding to each cell, where each MALDI-MSI pixel is weighted by how many IMC pixels are mapping to it. It is important to note that one MALDI-MSI pixel y_j may contribute to the expression of one or more cells.

Data analysis
Cellular phenotypes and metabolite abundance per cell were combined using Python (version 3.9), and metabolite abundance counts were normalized to the relative abundance per cell. RStudio was used for visualization and consecutive analyses. For each sample, data from two images were combined and mean relative metabolite abundance was determined for each cellular phenotype and visualized in a heatmap per sample using the ComplexHeatmap R package (version 2.14.0). Differential feature expression analysis was done by Wilcoxon rank test on the group of interest versus the remaining cells in the dataset and visualizing the features by fold change and P value. Finally, for dimensionality reduction, the cells were visualized by UMAP[28] using the umap R package (version 0.2.10.0) using the parameters n_neighbors of 5, min_dist of 0.05 and n_epochs of 1,000, and cell phenotypes or k-means clusters were visualized on the embedding.

Statistics
As a methodological proof of principle, the study was conducted on three CRC tissue samples, with two areas imaged per sample. Differentially abundant metabolites were identified using the Wilcoxon test, and features with a false discovery rate (FDR)-adjusted P value below 0.05 were considered significant.

Reporting summary
Further information on research design is available in the Nature Portfolio Reporting Summary linked to this article.

Data availability
Raw IMC and MSI data as well as combined datasets and source data are available via figshare at https://figshare.com/s/c58ddc-70fa8dc0602842 (ref. 29). Source data are provided with this paper.

Code availability
Python scripts used for the coregistration and integration of MALDI-MSI and IMC data are available on GitHub at https://github.com/deMirandaLab/MALDI-MSI-IMC.

References
26. Wishart, D. S. et al. HMDB 5.0: the Human Metabolome Database for 2022. *Nucleic Acids Res.* **50**, D622–D631 (2022).
27. Guo, N. et al. A 34-marker panel for imaging mass cytometric analysis of human snap-frozen tissue. *Front. Immunol.* **11**, 1466 (2020).
28. McInnes, L., Healy, J., Saul, N. & Großberger, L. UMAP: uniform manifold approximation and projection. *J. Open Source Softw.* **3**, 861 (2018); https://doi.org/10.21105/joss.00861
29. Ijsselsteijn, M. Supplementary files MALDI-MSI_IMC_CRC data integration. *figshare* https://doi.org/10.6084/m9.figshare.23599044.v1 (2024).

Author contributions
Conceptualization and funding was carried out by by N.F.F.C.d.M. and B.H. Experiments were performed by J.B.N., M.E.I., R.U. and M.v.d.P. Data analysis was done by M.E.I., T.A., A.M. and B.H. Writing was done by J.B.N. and M.E.I. The study was supervised by M.G., B.E., A.M., B.H. and N.F.F.C.d.M. Writing—review and editing was carried out by A.M., B.H. and N.F.F.C.d.M. Approval of the final version of the paper was carried out by all authors.

Competing interests
B.H. is presently employed by Bruker Corporation; however, this affiliation was not in place at the time of submission. The other authors declare no competing interests.

Additional information
**Extended data** is available for this paper at https://doi.org/10.1038/s41592-024-02392-6.

Supplementary information The online version contains supplementary material available at https://doi.org/10.1038/s41592-024-02392-6.

Correspondence and requests for materials should be addressed to Noel F. C. C. de Miranda.

Peer review information *Nature Methods* thanks Sean Bendall, Carsten Hopf, Roland Nilsson and the other, anonymous, reviewer(s) for their contribution to the peer review of this work. Peer reviewer reports are available. Primary Handling Editor: Madhura Mukhopadhyay, in collaboration with the *Nature Methods* team.

**Reprints and permissions information** is available at www.nature.com/reprints.
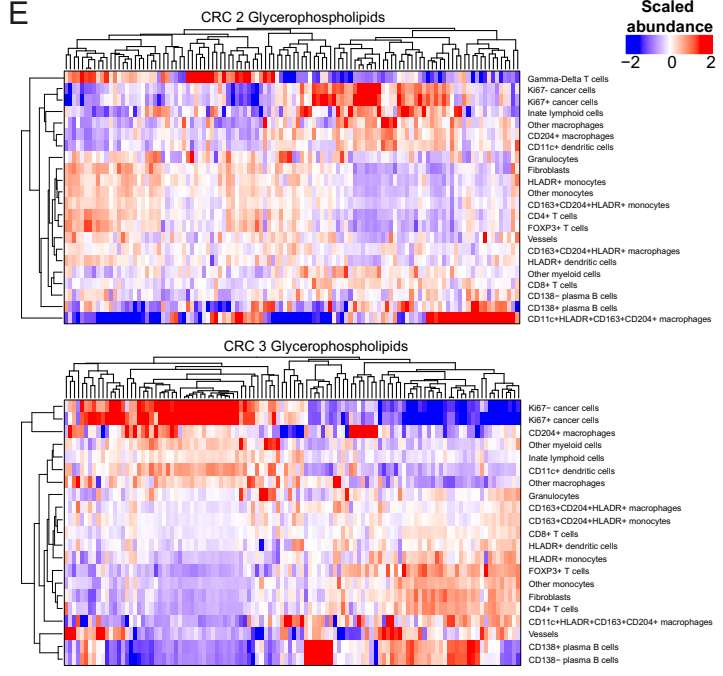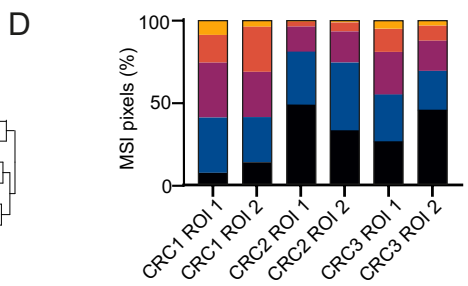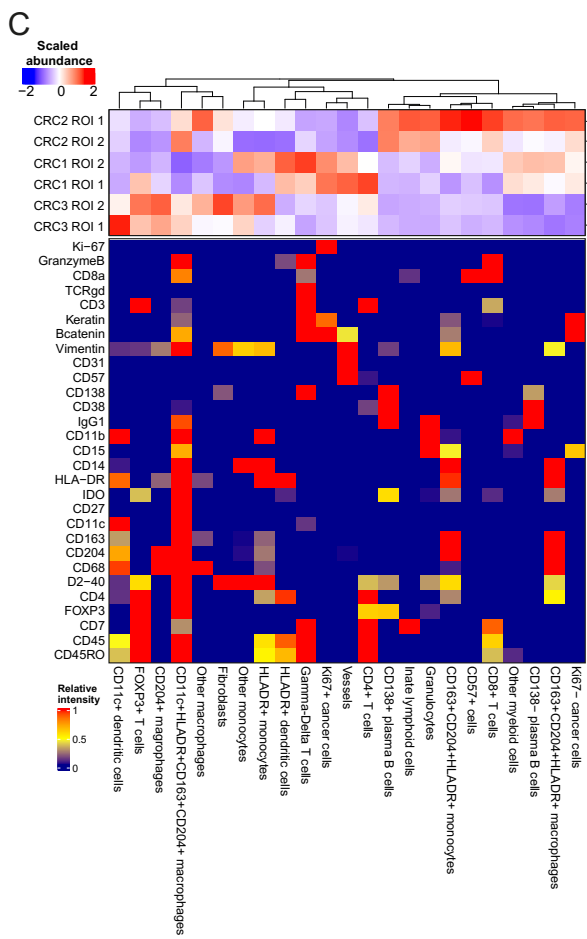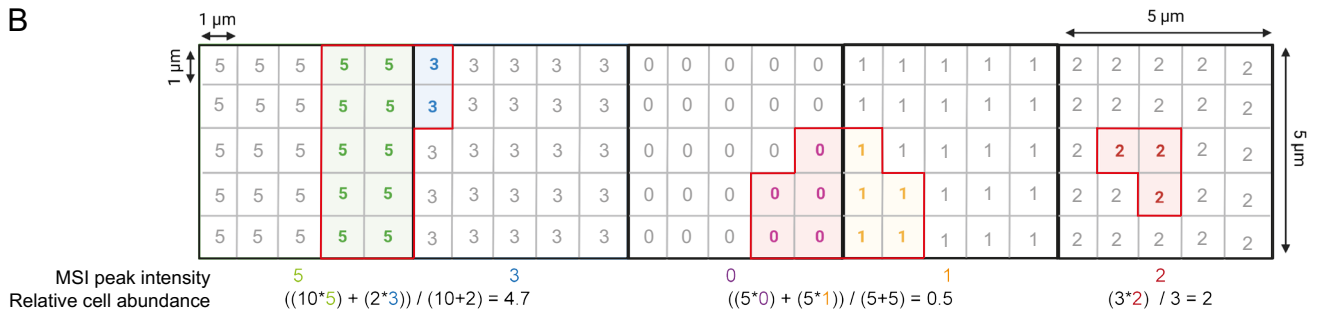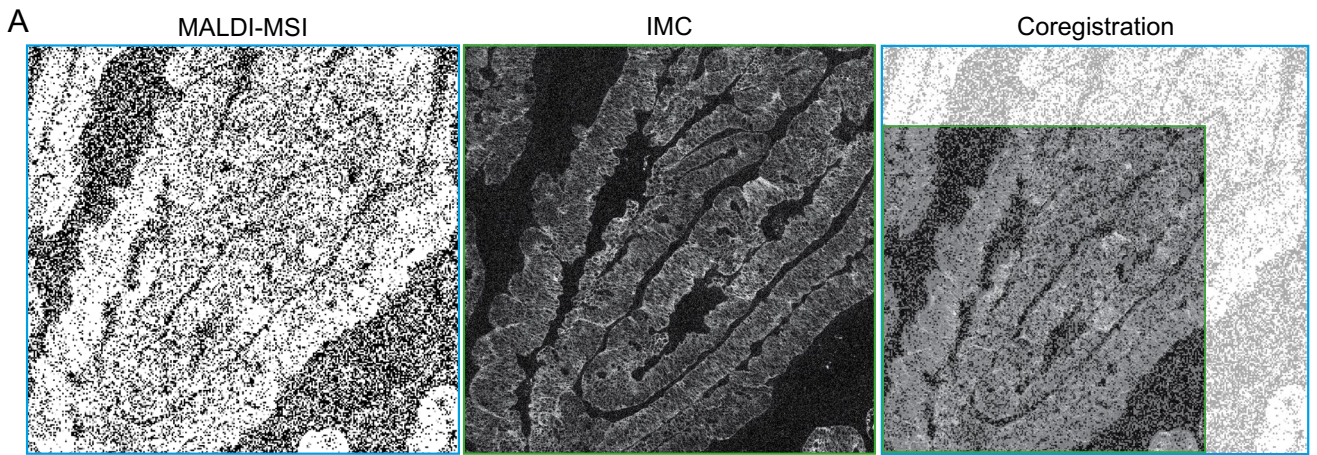
Extended Data Fig. 1 | See next page for caption.

Extended Data Fig. 1 | Integration of MALDI-MSI metabolite data with cellular phenotypes. a. Approach for aligning MALDI-MSI and IMC data using visual landmarks present in both datasets. **b**. Schematic illustrating the approach for calculating metabolite abundance in each cell as pixel sizes differ between MALDI-MSI and IMC. Five 5 × 5 µm MALDI-MSI pixels are shown, each containing 25 1 × 1 µm IMC pixels. Cells within the pixels are colored with a red border, and a cell can span multiple MALDI-MSI pixels. To calculate metabolite abundance per cell, the peak intensity of the overlapping 5 × 5 µm MALDI-MSI pixel was assigned to each 1 × 1 µm IMC-pixel. The IMC cell segmentation mask (red borders) and the assigned peak intensities of each 1 × 1 µm were combined, and the relative metabolite abundance per cell was calculated using the mean of all pixels within a cell. **c**. Relative marker expression and abundance per image of cellular phenotypes determined by IMC. **d**. distribution of the number of cells contained in a single MSI pixel for each image. **e**. Glycerophospholipid profiles across distinct cellular phenotypes, in CRC2 and CRC3. Hierarchical clustering was guided by glycerophospholipid abundances.
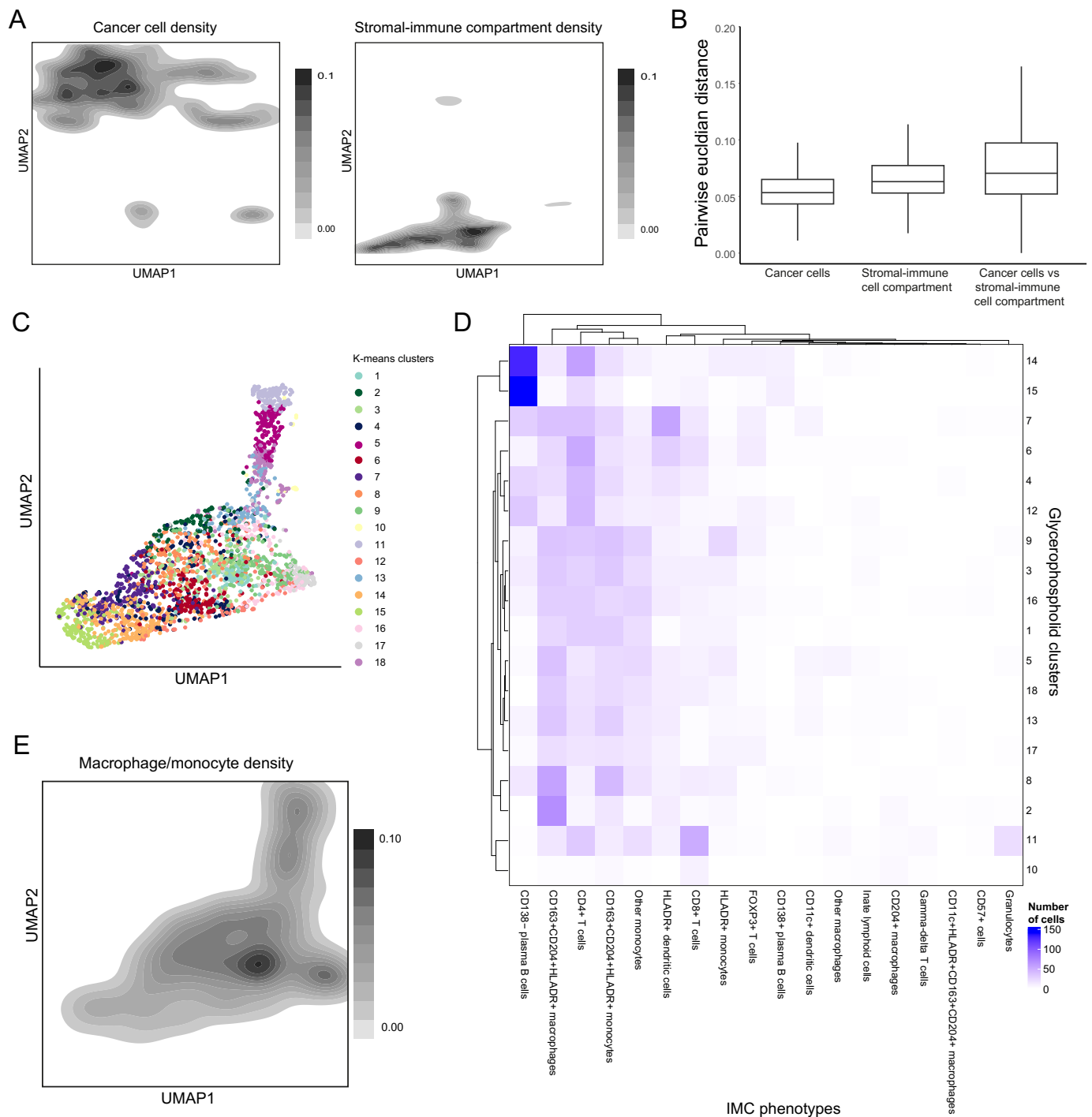
Extended Data Fig. 2 | Glycerophospholipid heterogeneity within cell populations. a. Density of cancer cell phenotypes and immune/stromal phenotypes corresponding to the UMAP of Fig. 1c. **b**. Pairwise distances between cancer cells, cancer cells and the stromal/immune compartment or the stromal/immune compartment only, visualized in a boxplot with median distance, interquartile range and min-max whiskers. n = 9066 cancer cells and 4889 stromal/immune cells. **c**. k-means clustering of all immune cells in CRC1 based on glycerophospholipid features, visualized on the UMAP embedding shown in Fig. 1d. **d**. Confusion matrix comparing IMC phenotypes with k-means clusters to determine clustering by cell type or glycerophospholipid features. The heatmap indicates the number of cells that overlap between the two clustering methods. **e**. Density of CD204⁺ macrophage phenotypes corresponding to the UMAP of Fig. 1d.
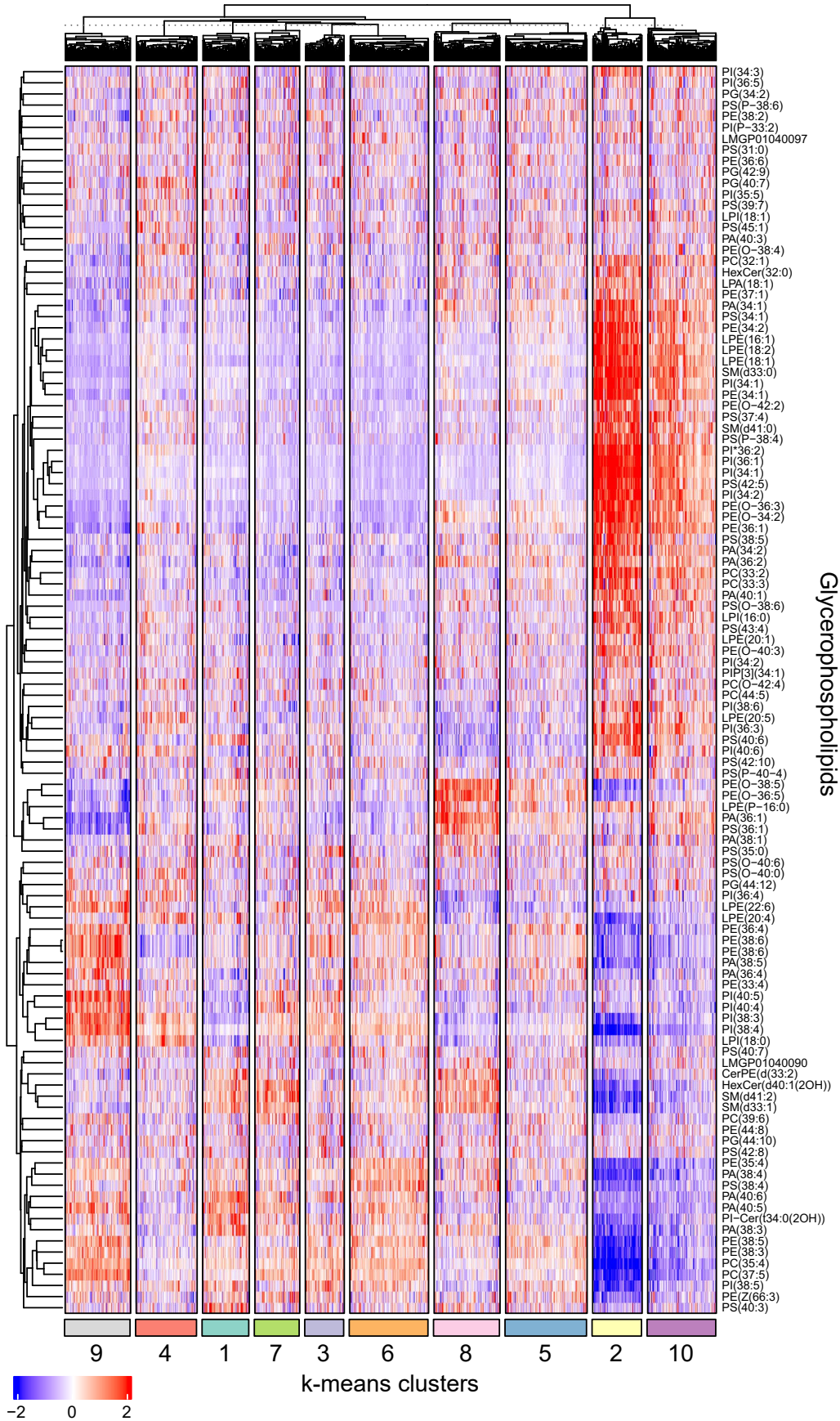
Extended Data Fig. 3 | Glycerophospholipid abundance in myeloid cell k-means clusters. Enlarged heatmap of Fig. 2e: Relative abundance of glycerophospholipids in the k-means clusters, visualized in Fig. 2d.

nature portfolio

Corresponding author(s): Noel de Miranda

Last updated by author(s): 18/01/2024

Reporting Summary

Nature Portfolio wishes to improve the reproducibility of the work that we publish. This form provides structure for consistency and transparency in reporting. For further information on Nature Portfolio policies, see our Editorial Policies and the Editorial Policy Checklist.

Statistics

For all statistical analyses, confirm that the following items are present in the figure legend, table legend, main text, or Methods section.

n/a	Confirmed	
☐	☒	The exact sample size (*n*) for each experimental group/condition, given as a discrete number and unit of measurement
☒	☐	A statement on whether measurements were taken from distinct samples or whether the same sample was measured repeatedly
☐	☒	The statistical test(s) used AND whether they are one- or two-sided *Only common tests should be described solely by name; describe more complex techniques in the Methods section.*
☒	☐	A description of all covariates tested
☒	☐	A description of any assumptions or corrections, such as tests of normality and adjustment for multiple comparisons
☐	☒	A full description of the statistical parameters including central tendency (e.g. means) or other basic estimates (e.g. regression coefficient) AND variation (e.g. standard deviation) or associated estimates of uncertainty (e.g. confidence intervals)
☐	☒	For null hypothesis testing, the test statistic (e.g. *F*, *t*, *r*) with confidence intervals, effect sizes, degrees of freedom and *P* value noted *Give P values as exact values whenever suitable.*
☒	☐	For Bayesian analysis, information on the choice of priors and Markov chain Monte Carlo settings
☒	☐	For hierarchical and complex designs, identification of the appropriate level for tests and full reporting of outcomes
☒	☐	Estimates of effect sizes (e.g. Cohen's *d*, Pearson's *r*), indicating how they were calculated

Our web collection on statistics for biologists contains articles on many of the points above.

Software and code

Policy information about availability of computer code

Data collection	Data obtained using flexImaging software (v7.2, Bruker Daltonics GmbH) and CyTOF software (7.0.5189, Standard Biotools)
Data analysis	Imaging data was merged in Python (version 3.9) and further analyses and visualisation with R (version 4.3.3) in R-studio (version 2023-1-12) using the following R packages: ComplexHeatmap (version 2.14.0), umap (version 0.2.10.0). code avaible on https://github.com/deMirandaLab/MALDI-MSI-IMC

For manuscripts utilizing custom algorithms or software that are central to the research but not yet described in published literature, software must be made available to editors and reviewers. We strongly encourage code deposition in a community repository (e.g. GitHub). See the Nature Portfolio guidelines for submitting code & software for further information.

Data

Policy information about availability of data

All manuscripts must include a data availability statement. This statement should provide the following information, where applicable:

- Accession codes, unique identifiers, or web links for publicly available datasets
- A description of any restrictions on data availability
- For clinical datasets or third party data, please ensure that the statement adheres to our policy

Raw IMC and MSI data as well as combined datasets and source data are available via figshare: https://figshare.com/s/c58ddc70fa8dc0602842

Human research participants

Policy information about studies involving human research participants and Sex and Gender in Research.

Reporting on sex and gender	Data not collected
Population characteristics	NA
Recruitment	NA
Ethics oversight	Medical Ethical Committee of the Leiden University Medical Centre

Note that full information on the approval of the study protocol must also be provided in the manuscript.

Field-specific reporting

Please select the one below that is the best fit for your research. If you are not sure, read the appropriate sections before making your selection.

☒ Life sciences   ☐ Behavioural & social sciences   ☐ Ecological, evolutionary & environmental sciences

For a reference copy of the document with all sections, see nature.com/documents/nr-reporting-summary-flat.pdf

Life sciences study design

All studies must disclose on these points even when the disclosure is negative.

Sample size	Three samples, as the study is a methodological proof of principle. no differences were observed between samples and thus not more samples were included
Data exclusions	no data excluded
Replication	2 areas imaged per sample, no areas or samples were discarded
Randomization	NA, no groups involved
Blinding	samples were anonimised and analysed as such

Reporting for specific materials, systems and methods

We require information from authors about some types of materials, experimental systems and methods used in many studies. Here, indicate whether each material, system or method listed is relevant to your study. If you are not sure if a list item applies to your research, read the appropriate section before selecting a response.

Materials & experimental systems

n/a	Involved in the study
☐	☒ Antibodies
☒	☐ Eukaryotic cell lines
☒	☐ Palaeontology and archaeology
☒	☐ Animals and other organisms
☒	☐ Clinical data
☒	☐ Dual use research of concern

Methods

n/a	Involved in the study
☒	☐ ChIP-seq
☒	☐ Flow cytometry
☒	☐ MRI-based neuroimaging

Antibodies

Antibodies used	CD4 EPR6855 Abcam CD8a D8A8Y Cell Signaling Technology ICOS D1K2T Cell Signaling Technology CD204 J5HTR3 Thermofisher Scientific CD163 D6U1J Cell Signaling Technology HLA-DR TAL 1B5 Abcam CD11b D6X1N Cell Signaling Technology

Granzyme B D6E9W Cell Signaling Technology
CD138 MI15 Biolegend
CD14 D7A2T Cell Signaling Technology
CD7 EPR4242 Abcam
CD11c EP1347Y Abcam
CD45 D9M8I Cell Signaling Technology
CD3 EP449E Abcam
FOXP3 D608R Cell Signaling Technology
CD27 EPR8569 Abcam
Vimentin D21H3 Cell Signaling Technology
Keratin C11 Cell signaling Technology
Keratin AE1/AE3 Biolegend
CD68 D4B9C Cell Signaling Technology
CD31 89C2 Cell Signaling Technology
CD57 HNK-1 / Leu-7 Abcam
Ki-67 8D5 Cell Signaling Technology
IgG1 EPR4417 Abcam
CD45RO UCHL1 Cell Signaling Technology
D2-40 D2-40 Biolegend
CD38 EPR4106 Abcam
Histone H3 D1H2 Cell Signaling Technology

Validation

All antibodies were selected based on thorough validation by the selling companies for human specificity and validated use for FFPE IHC. Antibodies were further tested in house by IHC and by multiplex imaging mass cytometry as shown in Ijsselsteijn et al 2019 (10.3389/fimmu.2019.02534) to confirm colocalisation with literature defined co expressed proteins.